PNAS RESEARCH ARTICLE | CHEMISTRY

Thermodynamic properties and enhancement of diamagnetism in nitrogen doped lutetium hydride synthesized at high pressure

Yifeng Han[a,1], Yunbo Ou[b,1], Hualei Sun[c], Jan Kopaczek[b,d], Gerson J. Leonel[a], Xin Guo[e], Benjamin L. Brugman[a], Kurt Leinenweber[a], Hongwu Xu[a], Meng Wang[f], Sefaattin Tongay[b,2], and Alexandra Navrotsky[a,b,2]

Contributed by Alexandra Navrotsky; received December 8, 2023; accepted February 12, 2024; reviewed by Maria Huffman and Zi-Kui Liu

Nitrogen doped lutetium hydride has drawn global attention in the pursuit of room-temperature superconductivity near ambient pressure and temperature. However, variable synthesis techniques and uncertainty surrounding nitrogen concentration have contributed to extensive debate within the scientific community about this material and its properties. We used a solid-state approach to synthesize nitrogen doped lutetium hydride at high pressure and temperature (HPT) and analyzed the residual starting materials to determine its nitrogen content. High temperature oxide melt solution calorimetry determined the formation enthalpy of $LuH_{1.96}N_{0.02}$ (LHN) from LuH_2 and LuN to be −28.4 ± 11.4 kJ/mol. Magnetic measurements indicated diamagnetism which increased with nitrogen content. Ambient pressure conductivity measurements observed metallic behavior from 5 to 350 K, and the constant and parabolic magnetoresistance changed with increasing temperature. High pressure conductivity measurements revealed that LHN does not exhibit superconductivity up to 26.6 GPa. We compressed LHN in a diamond anvil cell to 13.7 GPa and measured the Raman signal at each step, with no evidence of any phase transition. Despite the absence of superconductivity, a color change from blue to purple to red was observed with increasing pressure. Thus, our findings confirm the thermodynamic stability of LHN, do not support superconductivity, and provide insights into the origins of its diamagnetism.

thermodynamic | drop solution calorimetry | high pressure and high temperature | solid-state chemistry

Significance

This study examines the physical properties and fundamental thermodynamics of nitrogen doped lutetium hydride (LHN), which was recently reported to exhibit superconductivity at pressure near 1 GPa. Employing high temperature, high pressure solid-state synthesis, we quantified nitrogen doping in LHN. Drop solution calorimetry indicates a formation enthalpy for LHN of −28.4 ± 11.4 kJ/mol. Extensive conductivity tests were conducted up to 26.6 GPa, alongside optical and Raman spectroscopy up to 13.7 GPa but no superconductivity or structural phase transitions were observed in LHN. However, increased nitrogen content in LHN does markedly enhance its diamagnetic properties. These results contribute to understanding the thermodynamic, magnetic, and electronic behaviors of nitrogen doped hydrides, but do not support previous reports of superconductivity in LHN.

The pursuit of room-temperature superconductors has resulted in the development of materials with progressively higher superconducting temperatures (1). The development of hydrogen-rich superconductors at high pressure based on Bardeen–Cooper–Schrieffer and Migdal–Eliashberg theory has pushed the maximum superconducting temperature above 200 K (2, 3). Examples include H_3S, with a superconducting transition temperature (T_c) of 203 K at 155 GPa (4), LuH_{10} with T_c = 250 K at 170 GPa (5, 6), and (La, Y)H_{10} with T_c = 253 K at 183 GPa (7). While the highest superconducting transition temperature has been increased with the development of new materials, near-room-temperature superconductivity has remained out of reach, with one of the major hurdles being synthesis conditions at hundreds of GPa pressure.

Recently, room-temperature (294 K) superconductivity was reported in the Lu-H-N system at pressures near 1 GPa (8). Diamagnetism and heat capacity reported for the material also support a superconducting transition near room temperature, which is accompanied by a color change with increasing pressure, from dark blue to pink to red. Superconductivity was reported only for the pink phase (for P ~ 0.3-3 GPa) (8).

These reports have generated both interest and controversy (9–15). Ming et al. (9) and Xing et al. (14) synthesized $LuH_{2\pm x}N_y$ using a large volume press, and while the synthesis method was different from that used by Dias (8), the powder X-ray diffraction (PXRD) data and pressure modulated color changes were similar (8). However, neither study resulted in superconducting $LuH_{2\pm x}N_y$ and magnetic measurements instead indicated a paramagnetic phase which is more consistent with LuH_2 (11).

Synthesis of Lu-H-N by high pressure has primarily been achieved with H_2/N_2 in diamond anvil cells (DACs) or by using NH_4Cl and CaH_2 as N and H sources in large-volume press. It is impossible with these methods to determine how much N actually enters the LuH_2, or even whether it enters the LuH_2 lattice rather than being adsorbed onto the surface. In this work, we conducted HPT synthesis of $LuH_{1.96}N_{0.02}$, constrained its nitrogen content by using well-defined starting materials in a closed system, characterized its crystal structure, determined its formation enthalpy, and measured its magnetic properties and electrical conductivity.

Author contributions: Y.H. and Y.O. designed research; Y.H., H.S., J.K., and M.W. performed research; Y.H., Y.O., H.S., J.K., G.J.L., X.G., B.L.B., K.L., H.X., M.W., S.T., and A.N. analyzed data; S.T. and A.N. supervised research; and Y.H., Y.O., B.L.B., and A.N. wrote the paper.

Reviewers: M.H., University of Washington; and Z.-K.L., The Pennsylvania State University.

The authors declare no competing interest.

[1]Y.H. and Y.O. contributed equally to this work.

[2]To whom correspondence may be addressed. Email: sefaattin.tongay@asu.edu or alexandra.navrotsky@asu.edu.

This article contains supporting information online at https://www.pnas.org/lookup/suppl/doi:10.1073/pnas.2321540121/-/DCSupplemental.

Published March 14, 2024.

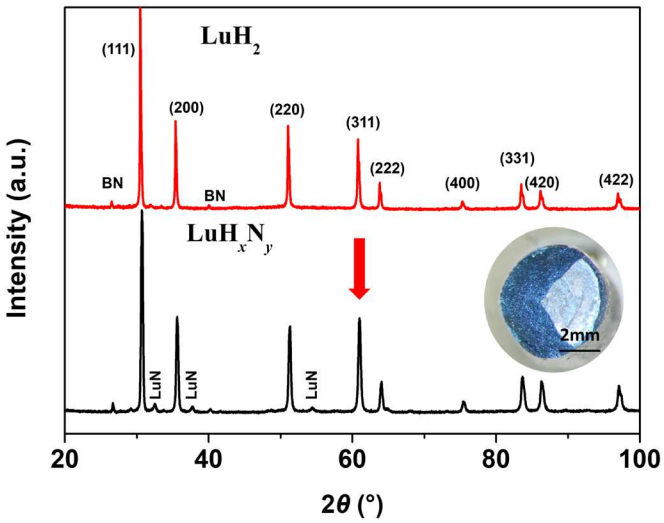

Fig. 1. PXRD data for LuH_2 and LHN after heating to 1273 K at 5 GPa. The red arrow marks the (311) diffraction peak of LHN, which is significantly enhanced in relative intensity compared to LuH_2. The inset is a picture of LHN.

Results and Discussion

Crystal Structure and Determination of N Content. PXRD patterns for LuH_2 and LHN after the high pressure experiment are provided in Fig. 1. The inset is a photograph of blue LHN at ambient pressure after removal from the multianvil press. In comparison to LuH_2, the relative intensity of the diffraction peaks of LHN varies, with the (311) peak showing the most significant enhancement, we attribute this change in relative intensity to preferred orientation or stacking faults caused by nitrogen doping. The lattice parameter and volume of LHN decrease compared to LuH_2, reducing from 5.0381(1) Å to 5.03411(6) Å and from 127.885(7) $Å^3$ to 127.576(5) $Å^3$, respectively. Light elements are hard to quantify by X-ray diffraction, therefore the N content cannot be obtained by refinement, so we estimate the nitrogen content in LHN by calculating the content of the LuN phase (2.8 wt %) from Rietveld refinement (*SI Appendix*, Fig. S1 and Table S1) combined with the ratio of LuH_2 and LuN in the precursor (19:1). The calculated chemical formula of our synthesized LHN phase is $LuH_{1.96}N_{0.02}$. X-ray photoelectron spectroscopy (XPS) measurement (*SI Appendix*, Fig. S2) indicates the presence of nitrogen in the material. However, due to the weak signal from the low doping level of nitrogen, it is not possible to analyze the state of N by XPS. The magnetic analysis of $LuH_{2\pm x}N_y$ with different nitrogen doping levels further confirms that nitrogen has been successfully doped into LuH_2.

Thermodynamics. The drop solution enthalpies for LuH_2 and LHN determined from high temperature oxide melt solution calorimetry are –695.45 ± 7.89 kJ/mol and –663.62 ± 7.50 kJ/mol, respectively. Thermochemical cycles are given in Table 1, and individual enthalpy values are provided in *SI Appendix*, Table S2. The enthalpy of formation (ΔH_f) for LHN from LuH_2 and LuN is –28.4 ± 11.4 kJ/mol, which supports stability relative to the constituent components LuH_2 and LuN, making decomposition unfavorable. Entropy effects, generally close to zero for solid-state reactions, are unlikely to change the trend of stability. To verify the incorporation of nitrogen we conducted N-doping experiments on LuH_2 in a N_2 dosing system. PXRD measurements indicate a significant change in the relative intensity of (311) peaks (*SI Appendix*, Fig. S3), which also indicates the successful doping of N in LuH_2 and supports the results of the drop solution calorimetry. Since the exact stoichiometry resulting from these experiments cannot be constrained, we used high pressure synthesized LHN to address the issue of undetermined N doping content and only the high pressure LHN was used for the electrical and magnetic measurements.

Table 1. Thermochemical cycle for calculation of enthalpy of formation of LHN ($\Delta H°_f$)

Reaction	ΔH (kJ mol^{-1})
LuH_2 (s, 298 K) + (3/4) O_2 (g, 1073K) → (1/2) Lu_2O_3 (soln, 1073 K) + H_2O (g, 1073K)*	ΔH_1 = −695.45 ± 7.89
LuN (s, 298 K) + (1/4) O_2 (g, 1073K) → (1/2) Lu_2O_3 (soln, 1073 K) + (1/2) N_2*	ΔH_2 = −525.84 ± 3.50
$LuH_{1.96}N_{0.02}$ (s, 298 K) + (1.24) O_2 (g, 1073K) → (1/2) Lu_2O_3 (soln, 1075K) + (0.98) H_2O (g, 1073K) + (0.01) N_2 (g, 1073K)*,†	ΔH_3 = −663.62 ± 7.53
0.98 LuH_2 (s, 298 K) + 0.02LuN (s, 298 K) → $LuH_{1.96}N_{0.02}$ (s, 298 K)	
$\Delta H°_f$ = 0.98 ΔH_1 + 0.02ΔH_2 -ΔH_3	$\Delta H°_f$ = −28.43 ± 11.43

*Value is the mean of the number of experiments indicated in parentheses. Two SD of the mean are given as errors.
†Chemical formula obtained by Rietveld refinement.

Thermochemical analysis indicates that LHN is thermodynamically stable relative to binary nitride and hydride, thus disfavoring spontaneous phase separation (decomposition) of the material into individual components LuH_2 and LuN. This stability suggests that the interfacial interactions between different local structures and/or energetics of formation of N or H defects in the structure are thermodynamically favorable, perhaps due to reduced lattice strain in the LuH_2 host structure, originating from the incorporation of N-Lu-H mixed bonds.

Magnetism. To further study how nitrogen doping affects the properties of the sample, we measured the magnetic properties of LuH_2, low N doped LHN (L-LHN), and LHN samples at 2 to 350 K. As the temperature decreases, the Zero-Field-Cooled (ZFC) and the Field-Cooled (FC) curves exhibit bifurcation below 300 K, shown in Fig. 2 *A*–*C*. After doping the sample with nitrogen, the plateau of the ZFC curve widens. This is typical behavior for a superparamagnetic material and/or a spin-glass system. The magnetic hysteresis loops were collected from 5 (or 2) to 350 K for different samples as illustrated in Fig. 2 *D*–*F*. Interestingly, the magnetization signal shows a sudden jump (dM/dH > 0.0017 emu/T) close to $\mu_0 H$ = 0 for all temperatures and samples. A closer look at the hysteresis loop in this range is shown in Fig. 2 *D*–*F*, *Insets*. The extracted remanent magnetization (M_r) and coercive field (H_c) are plotted in Fig. 2 *G*–*I* as a function of temperature and show similar temperature response. While M_r and H_c are independent of temperature for LuH, they generally decrease with increasing temperature for L-LHN and LHN. The remanent magnetization is strongly suppressed for higher nitrogen doping (LHN). We attribute the observed differences in M_r(T) and H_c(T) between undoped and doped samples to the emergence of diamagnetism caused by diamagnetic N centers. More explicitly, as the N doping increases, the diamagnetic contribution from these diamagnetic N defect centers contributes more to the overall measured magnetism which can be seen from the increased negative slope in the *MH* loops as shown in Fig. 2 *D*–*F*. The diamagnetic contribution was quantified by extracting the slope of each *M*-*H* curve from 5 T to 6.9 T, where the linear portion can be seen as shown in Fig. 2*H*. The results show that the

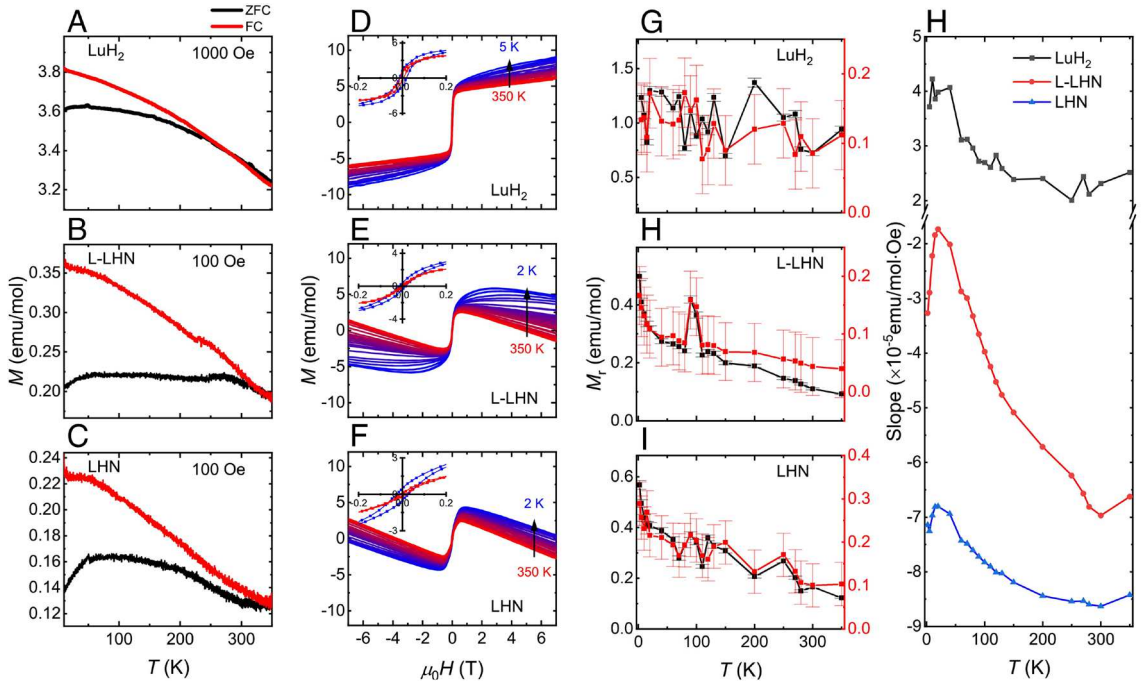

Fig. 2. The magnetic properties of LuH_2, L-LHN, and LHN. (*A–C*) The ZFC and FC curves of LuH_2, L-LHN, and LHN, respectively, in the presence of a small magnetic field. (*D–F*) The loop scan of the *M-H* curve at elevated temperatures. The *Inset* is the zoom-in of the *M-H* curve at the lowest and highest temperatures. (*G–I*) The M_r and H_c as a function of temperature extracted from *D–F*. The error bars of M_r and H_c come from the instrument error and half of adjacent data points. (*H*) The temperature dependence of slope by linear fitting from 5 T to 6.9 T extracted from *D–F*.

diamagnetic signal is enhanced at low temperatures and suppresses the superparamagnetism.

Electrical Conductivity. Electrical transport measurements were carried out to determine the resistivity of the samples at different temperatures and external magnetic fields. Temperature-dependent longitudinal resistivity $\rho(T)$ curves under an increasing external magnetic field up to 7 T are shown in Fig. 3*A*. Generally, the resistivity during cool-down and warm-up processes should trace each other with an adequate temperature ramping rate. However, hysteretic behavior was observed in our LHN sample (*SI Appendix*, Fig. S4*A*), which has also been observed elsewhere (14) and in LuH_2 crystals (13) and has been explained as a percolation effect. Because the warm-up process is in thermal equilibrium, these curves are shown in Fig. 3*A*. The $\rho(T)$ curves indicate that our LHN behaves as a typical metal. Under an external magnetic field (Fig. 3*B*), a bump in the resistivity curve appears around 263 K. After subtracting the $\rho(T)$ curve at $\mu_0 H = 0$ T, a stronger

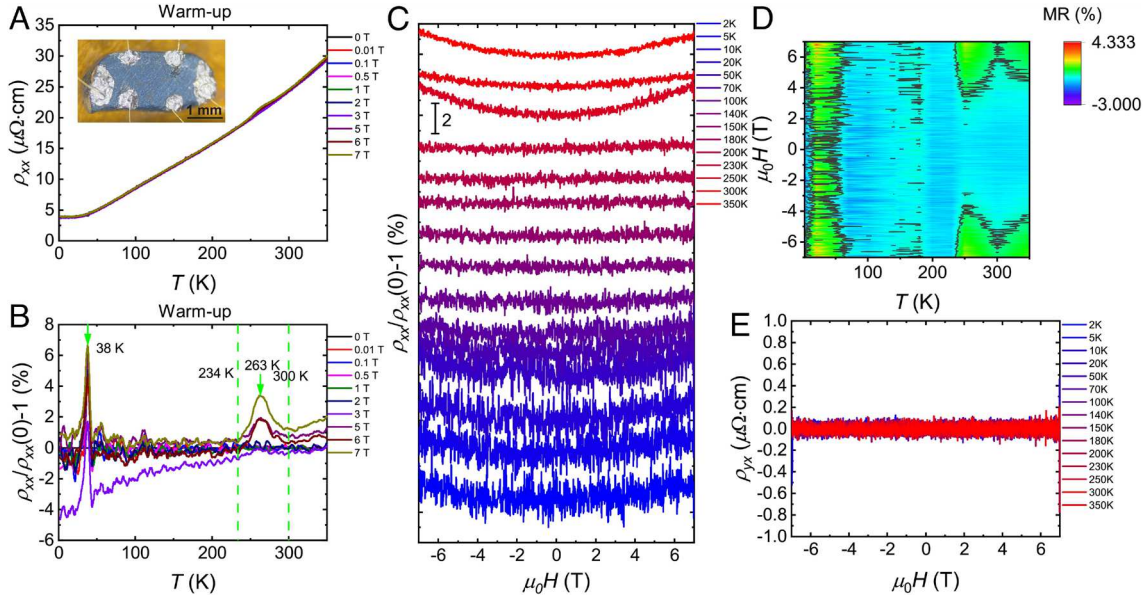

Fig. 3. The electrical properties of LHN. (*A*) The temperature dependence of resistivity at different magnetic fields in the warm-up process. The *Inset* is the optical image of the device used in the measurement. (*B*) The temperature dependence of resistivity at different magnetic fields by subtracting the curve at 0 T. (*C*) The magnetoresistance at elevated temperatures from 2 K to 350 K. The data is offset. (*D*) The contour plot of magnetoresistance as a function of temperature and magnetic field converted from Fig. 3*C*. The gray line marks MR = 0.2%. (*E*) The Hall resistivity as a function of the magnetic field at elevated temperatures.

magnetic response of resistivity appears above 234 K. This response delineates a curve which peaks at 263 K, decreases until 300 K and then increases linearly to 350 K. Additionally, a sharp peak at 38 K is associated with a sudden change of resistivity when $\mu_0 H = 0$ T. This change disappears when a small field ($H = 0.01$ T) is applied (*SI Appendix*, Fig. S4*B*). These sudden changes in $\Delta\rho/\rho$ are usually associated with structural changes (possible phase transitions) or complex strain relaxation processes due to structural texture and warrant future studies (16).

To further study the effects of the magnetic field on resistivity, we conducted magnetoresistivity (MR) and Hall resistivity measurements at elevated temperatures. As shown in Fig. 3*C*, a weak parabolic MR behavior is seen at $T < 70$ K and MR remains constant from 70 to 250 K as the temperature is increased. Above 250 K, parabolic MR emerges (~2% MR at 7 T). The observed MR at high temperatures is also consistent with the ρ(T) plots under a magnetic field in Fig. 3*A*. The enhancement in MR above 250 K can be easily identified from the contour plots of MR (Fig. 3*D*). Due to the metallic nature of the sample, the parabolic MR manifests the topology of the Fermi surface (17). A constant/parabolic MR generally represents a closed/open electron/hole orbit (18). The Hall resistivity was measured to 2 K, but no detectable Hall signal was present within the limit of our measurements, confirming that the sample is a good metal with high conductivity (Fig. 3*E*).

Fig. 4 depicts the change of resistance with temperature for LHN across the pressure range of 0.5 to 26.6 GPa. We note that the pressure-dependent electrical measurements were collected from the same sample (LHN) used for electrical measurements at ambient pressure. Results show that initial small pressure ($P = 0.5$ GPa and $P = 3.4$ GPa) induces a metal-to-semiconductor transition. As the pressure increases further, LHN undergoes a semiconductor-to-metal transition above 3.4 GPa, similar to that previously reported in $La_3Ni_2O_7$ (19). We note that even though the overall resistance was reduced, no superconducting transition was observed for pressures up to 26.6 GPa. When an external magnetic field of 10 T was applied at 26.6 GPa, there was no significant change in the resistance of the material in the 150 to 300 K range, but there was an increase in resistance in the 2 to 150 K range.

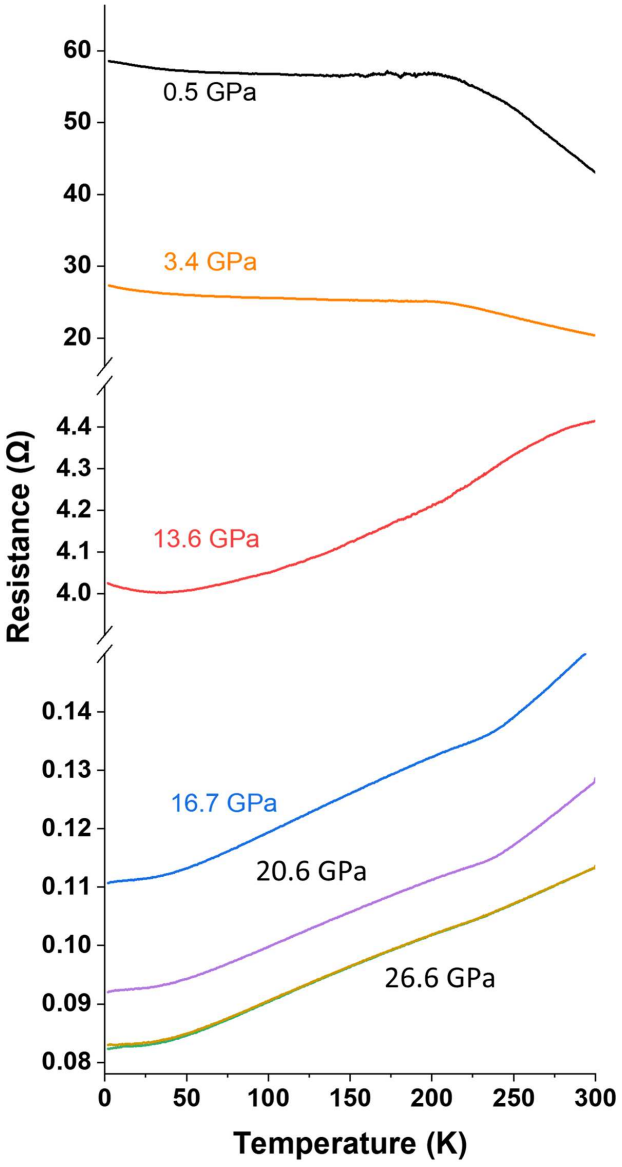

Fig. 4. Resistance of LHN versus temperature at different pressures from 0.5 GPa to 26.6 GPa.

Pressure-dependent Raman Spectra and Color Change. One of the most remarkable phenomena reported for LHN is the change in color from dark blue to pink to red with increasing pressure (9, 10, 13, 14). Previous studies have claimed that the pink region corresponds to the superconducting state for LHN (8). We applied gradual pressure to LHN up to 13.7 GPa in a DAC to observe the color changes and associate them with the overall electrical resistivity behavior (Fig. 4). Results from optical DAC measurements are shown in Fig. 5. As the pressure was increased to 11.7 GPa, the color of the LHN sample gradually changed from blue to purple and then to red. No further color change was observed between 11.7 and 13.7 GPa, and similar trends were observed during controlled pressure release. Overall results are in line with previous reports (9, 10, 13, 14), although there are some differences in the intermediate transition colors and transition pressures at which these changes occur. They may be attributable to differences in N content in LHN.

Raman data collected at each pressure step in the DAC are presented in *SI Appendix*, Fig. S5 *A* and *D*. No significant alteration in the Raman mode positions were observed in crystals with and without nitrogen. The positions of Raman modes observed at ~250 and 1,200 cm^{-1} are in good agreement with previously reported results (9, 10, 13, 14). Within the pressure range examined, no indications of phase change were observed and as pressure was increased, only a linear blueshift was observed in the Raman modes. The analysis of pressure-dependent reflectivity (*SI Appendix*, Fig. S5 *B* and *E*) supports the observed color change in Fig. 5. The slope of the reflectivity spectra (after smoothing, see *SI Appendix*, Fig. S5 *C* and *E*), allowed us to estimate the shift in plasma edge with increasing pressure, which indicated no phase transitions below 13.7 GPa. While the overall results show that LHN behaves optically similarly to previously reported samples with different N concentrations, no superconductivity (from electrical transport measurements in the same pressure range) or phase transitions were seen in the same pressure range.

Summary and Outlook. The work reports the synthesis of nitrogen doped lutetium hydride using high pressure and high temperature. High temperature oxide melt solution calorimetric measurements on high pressure LHN suggest that LHN is thermodynamically stable and can be prepared at ambient pressure. Stability is supported by additional synthesis of nitrogen doped lutetium hydride using gas adsorption calorimetry. Comprehensive, magnetic and electrical

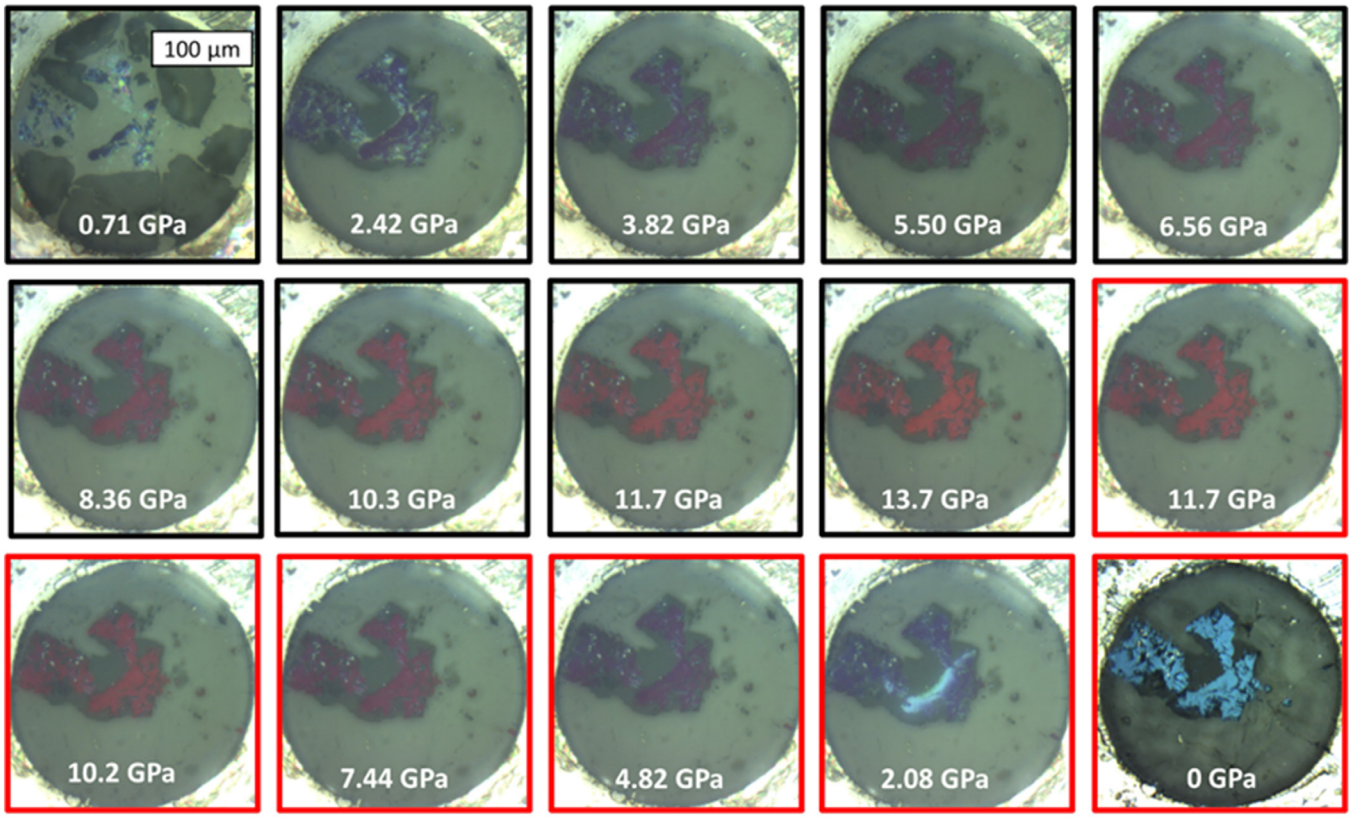

Fig. 5. Optical microscopy images of LHN material in a diamond anvil cell at pressures ranging from 0 to 13.7 GPa. The color of the LHN crystal shifts progressively from blue to red with increasing pressure and reverses from red to blue during decompression cycles. The black and red frames around images indicate the compression and decompression cycle, respectively.

measurements at ambient pressure, as well as high pressure electrical, Raman, and optical measurements establish physical properties of LHN in wide ranges of temperature, magnetic field, and pressure. Although our results point toward the absence of superconductivity in LHN at pressures up to 26.6 GPa, ambient pressure electrical transport measurements under magnetic field and under pressure point to the complexity of the Fermi surface topology. Future studies on the complex Fermi surface, crystal texture, and comprehensive doping engineering are needed to explore the conditions leading to possible superconductivity.

Materials and Methods

High Pressure Synthesis. LuH_xN_y precursor was prepared by mixing 19:1 (denoted as LHN) and 32:1 (denoted as L-LHN) molar ratios of LuH_2 (99.9%, VIILAA) and LuN in a glovebox. About 0.2 g of the LHN was packed in a BN capsule surrounded by a rhenium heater and loaded into an octahedral MgO-spinel 18/12 pressure assembly. The sample was compressed in a multianvil press with tungsten carbide anvils with corners truncated to 12 mm. The pressure was increased to 5 GPa over 6 h. The assembly was then heated to 1,273 K and held for 2 h before quenching to ambient temperature by cutting power to the heater. The pressure was reduced to ambient conditions for over 10 h, and the sample capsule was opened inside a glovebox under nitrogen. To obtain LuN, we heated Lu metal (40 mesh 99.8%, Alfa Aesar) under a nitrogen atmosphere at 1,273 K for 5 h in a controlled atmosphere furnace (Setaram-Labsys Evo).

Ambient pressure N doped LuH_2 was obtained by loading LuH_2 into a gas dosing system (Micromeritics ASAP 2020). The sample (~200 mg) was placed in one prong of a customized silica glass forked tube. The prongs of this tube were jacketed in the twin chambers of the calorimeter with the head opening connected to the gas dosing manifold. The sample was degassed under vacuum ($<2 \times 10^{-6}$ bar) at 773 K to remove any initial adsorbates. The gas dosing system was programmed in incremental dosing mode (5 µmol per dose).

Powder X-ray Diffraction. PXRD patterns were obtained using a Bruker D8 Advance diffractometer operated with Cu Kα radiation (λ = 1.54184 Å), a 1.0 mm air scatter screen, and a 0.6 mm divergence slit. The data were collected in the 2θ range of 28 to 110° with a step size of 0.01° and a dwell time of 5 s per step. Sample powders were transferred to an airtight PXRD holder inside the glovebox before transport to the diffractometer. Rietveld analyses of PXRD data were performed using Topas-Academic *V*6 software (20).

X-ray Photoelectron Spectroscopy. XPS experiments are performed by use of a Kratos AXIS Supra+ with a monochromatic Al K_α+ ion beam (beam energy = 1,486.6 eV).

High Temperature Oxide Melt Solution Calorimetry. High temperature oxide melt solution calorimetry experiments were carried out using a Setaram AlexSYS Tian-Calvet twin microcalorimeter using methods standard to our laboratory and described previously (21). The calorimeter was calibrated against the heat content of high purity α-Al_2O_3. Samples, each ~5 mg in weight were pelletized in a glovebox and transported to the calorimeter in closed centrifuge tubes under N_2 limiting contact with laboratory air to a few seconds. LHN pellets were then dropped from ambient temperature into the calorimeter containing molten sodium molybdate ($3Na_2O{\cdot}4MoO_3$) solvent at 1,073 K in a silica glass crucible. The dropping tubes were flushed with air at 75 mL min^{-1}, and oxygen was bubbled through the solvent at 35 mL min^{-1} to aid dissolution and prevent local saturation of the solvent. Complete oxidation and dissolution of the sample enabled measurement of the heat of dissolution under oxidizing conditions, from which formation enthalpies were determined.

Transport and Magnetic Measurements. Transport and magnetic measurements under ambient pressure were performed in a Quantum Design Physical Property Measurement System (PPMS, 1.9 K, 7 T). The electrodes were made by using gold wire electrodes with indium-pressed contacts. Keithley 6221 and SRS

830 instruments were used as the current source and as the nanovoltmeter for AC measurement with a driving current of 70 mA at 13 Hz frequency.

The electrical resistance measurements were carried out using the standard four-probe method. High pressure was generated with a screw-pressure-type DAC. Diamond anvils with a 400-μm culet were used, and the corresponding sample chamber with a diameter of 150 μm was made in an insulating gasket of cubic boron nitride and epoxy mixture. The pressure was calibrated using the ruby fluorescence shift at room temperature for all experiments. Electrical measurements were collected from 2 K to 300 K and magnetic fields up to 10 T using the PPMS.

High Pressure Raman Spectroscopy. LHN was compressed in a DAC with diamonds of 500 μm culet size and a steel gasket. Fine seeds of NaCl were used as a pressure-transmitting medium, and the pressure was determined based on the shift of the Raman mode from the diamond edge, which initially is located at 1,334 cm^{-1} at ambient pressure (22). Raman spectra were acquired in the backscattering configuration in a setup equipped with a 0.75-m focal-length Shemrock monochromator and a 532-nm CW laser. For improved spatial resolution, a laser line and white light (for reflectivity measurements) were focused using a 50× objective lens.

Data, Materials, and Software Availability. All study data are included in the article and/or *SI Appendix*.

ACKNOWLEDGMENTS. Sample synthesis, characterization, and calorimetry were supported by the U.S. Department of Energy, grant DE-SC0021987; S.T. acknowledges primary support from DOE-SC0020653 (materials characterization), NSF ECCS 2052527 (electrical characterization), and DMR 2111812 (optical characterization). We acknowledge the assistance of Facility for Open Research in a Compressed Environment (FORCE) staff members. The FORCE at ASU is funded by NSF-EAR under the Mid-scale Research Infrastructure-1 (2131833). We acknowledge the use of facilities within the Eyring Materials Center at Arizona State University supported in part by NNCI-ECCS-1542160. Work at SYSU was supported by the National Natural Science Foundation of China (12174454), the Guangdong Basic and Applied Basic Research Funds (2021B1515120015), Guangzhou Basic and Applied Basic Research Funds (202201011123), and the Guangdong Provincial Key Laboratory of Magnetoelectric Physics and Devices (2022B1212010008).

Author affiliations: [a]Center for Materials of the Universe, School of Molecular Sciences, Arizona State University, Tempe, AZ 85287; [b]School for Engineering of Matter Transport and Energy, Arizona State University, Tempe, AZ 85287; [c]School of Science, Sun Yat-Sen University, Shenzhen 518107, R.P. China; [d]Department of Semiconductor Materials Engineering, Faculty of Fundamental Problems of Technology, Wroclaw University of Science and Technology, Wrocław 50-370, Poland; [e]Eyring Materials Center, Arizona State University, Tempe, AZ 85287; and [f]Center for Neutron Science and Technology, Guangdong Provincial Key Laboratory of Magnetoelectric Physics and Devices, School of Physics, Sun Yat-Sen University, Guangzhou 510275, R.P. China

1. H. K. Onnes, The superconductivity of mercury. *Comm. Phys. Lab. Univ. Leiden* **122**, 124 (1911).
2. J. Bardeen, L. N. Cooper, J. R. Schrieffer, Theory of superconductivity. *Phys. Rev.* **108**, 1175 (1957).
3. P. B. Allen, R. Dynes, Transition temperature of strong-coupled superconductors reanalyzed. *Phys. Rev. B* **12**, 905 (1975).
4. A. Drozdov, M. Eremets, I. Troyan, V. Ksenofontov, S. I. Shylin, Conventional superconductivity at 203 kelvin at high pressures in the sulfur hydride system. *Nature* **525**, 73–76 (2015).
5. A. Drozdov *et al.*, Superconductivity at 250 K in lanthanum hydride under high pressures. *Nature* **569**, 528–531 (2019).
6. M. Somayazulu *et al.*, Evidence for superconductivity above 260 K in lanthanum superhydride at megabar pressures. *Phys. Rev. Lett.* **122**, 027001 (2019).
7. D. V. Semenok *et al.*, Superconductivity at 253 K in lanthanum–yttrium ternary hydrides. *Mater. Today Phys.* **48**, 18–28 (2021).
8. N. Dasenbrock-Gammon *et al.*, Evidence of near-ambient superconductivity in a N-doped lutetium hydride. *Nature* **615**, 244–250 (2023).
9. X. Ming *et al.*, Absence of near-ambient superconductivity in $LuH_{2\pm x}N_y$. *Nature* **620**, 72–77 (2023).
10. P. Shan *et al.*, Pressure-induced color change in the lutetium dihydride LuH_2. *Chin. Phys. Lett.* **40**, 046101 (2023).
11. S. Zhang *et al.*, Electronic and magnetic properties of Lu and LuH_2. *AIP Adv.* **13**, 065117 (2023).
12. M. Liu *et al.*, On parent structures of near-ambient nitrogen-doped lutetium hydride superconductor. arXiv [Preprint] (2023). https://doi.org/10.48550/arXiv.2303.06554 (Accessed 5 January 2023).
13. Y.-J. Zhang *et al.*, Pressure induced color change and evolution of metallic behavior in nitrogen-doped lutetium hydride. *Chin. Phys. Lett.* **66**, 287411 (2023).
14. X. Xing *et al.*, Observation of non-superconducting phase changes in $LuH_{2\pm x}N_y$. arXiv [Preprint] (2023). https://doi.org/10.48550/arXiv.2303.17587 (Accessed 5 January 2023).
15. Z. Li *et al.*, Superconductivity above 70 K observed in lutetium polyhydrides. *Sci. China Phys. Mech. Astron.* **66**, 267411 (2023).
16. D. Wu *et al.*, Ultrabroadband photosensitivity from visible to terahertz at room temperature. *Sci. Adv.* **4**, eaao3057 (2018).
17. S. Zhang, Q. Wu, Y. Liu, O. V. Yazyev, Magnetoresistance from Fermi surface topology. *Phys. Rev. B* **99**, 035142 (2019).
18. S. J. Blundell, "Magnetoresistance techniques applied to fermi surfaces" in *Encyclopedia of Condensed Matter Physics*, F. Bassani, G. L. Liedl, P. Wyder, Eds. (Elsevier, Oxford, 2005), pp. 253–261.
19. H. Sun *et al.*, Signatures of superconductivity near 80 K in a nickelate under high pressure. *Nature* **621**, 493–498 (2023).
20. A. A. Coelho, TOPAS and TOPAS-Academic: An optimization program integrating computer algebra and crystallographic objects written in C++. *J. Appl. Crystallogr.* **51**, 210–218 (2018).
21. A. Navrotsky, Progress and new directions in high temperature calorimetry revisited. *Phys. Chem. Miner.* **24**, 222–241 (1997).
22. Y. Akahama, H. Kawamura, Pressure calibration of diamond anvil Raman gauge to 310GPa. *J. Appl. Phys* **100**, 043516 (2006).